

Optics Letters

Endoscopic high-resolution autofluorescence imaging and OCT of pulmonary vascular networks

HAMID PAHLEVANINEZHAD,^{1,*} ANTHONY M. D. LEE,¹ GEOFFREY HOHERT,¹ STEPHEN LAM,¹
TAWIMAS SHAIPIANICH,¹ EVE-LEA BEAUDOIN,¹ CALUM MACAULAY,¹ CAROLINE BOUDOIX,² AND PIERRE LANE¹

¹Integrative Oncology Department, BC Cancer Research Center, 675 West 10th Avenue, Vancouver, British Columbia V5Z 1L3, Canada

²Polytechnique Montreal, Department of Engineering Physics, P.O. Box 6079 Station Centre-Ville, Montreal, Quebec H3C 3A7, Canada

*Corresponding author: hpahleva@bccrc.ca

Received 6 May 2016; revised 9 June 2016; accepted 13 June 2016; posted 13 June 2016 (Doc. ID 264015); published 7 July 2016

High-resolution imaging from within airways may allow new methods for studying lung disease. In this work, we report an endoscopic imaging system capable of high-resolution autofluorescence imaging (AFI) and optical coherence tomography (OCT) in peripheral airways using a 0.9 mm diameter double-clad fiber (DCF) catheter. In this system, AFI excitation light is coupled into the core of the DCF, enabling tightly focused excitation light while maintaining efficient collection of autofluorescence emission through the large diameter inner cladding of the DCF. We demonstrate the ability of this imaging system to visualize pulmonary vasculature as small as 12 μm *in vivo*. © 2016 Optical Society of America

OCIS codes: (170.0170) Medical optics and biotechnology; (170.0110) Imaging systems; (170.2520) Fluorescence microscopy; (170.4500) Optical coherence tomography.

<http://dx.doi.org/10.1364/OL.41.003209>

Vascular remodeling and angiogenesis have been associated with several lung diseases. The role of angiogenesis in enhancing tumor growth is widely accepted [1], and tumor vasculature is known to be structurally and functionally different from normal vessels [2]. Pulmonary hypertension due to vascular remodeling is a characteristic feature of chronic obstructive pulmonary disease (COPD) [3,4]. In addition, the visualization of vascular remodeling may provide structural features for the noninvasive identification of acute and chronic rejection following lung transplantation [5]. Thus, an imaging system capable of visualizing detailed pulmonary vascular networks *in vivo* could provide opportunities to study many different lung diseases and their pathological processes.

Optical coherence tomography (OCT) can visualize subluminal airway tissue structures at high resolution [6–8], and autofluorescence imaging (AFI) can probe fluorescent components of airway tissue such as collagen and elastin fibers [9–11]. Combined OCT–AFI may enable the detection and characterization of structural and functional features associated with different lung diseases.

In our previous work, we presented an endoscopic OCT–AFI instrument using a double-clad fiber (DCF) catheter, which is capable of detecting pulmonary nodules and vascular networks [12]. In this system, the DCF catheter core and inner-cladding carried the OCT and the AFI light, respectively [13]. However, this implementation limits AFI resolution because the AFI excitation light coupled to the large-diameter DCF inner cladding is not focused to a small spot size on the tissue.

This work presents a different implementation of OCT–AFI using fused fiber components [14–16] and a custom-designed fiber optic rotary joint (FORJ) that allows coupling AFI excitation into the core of the DCF catheter. In this implementation, a tightly focused AFI excitation light ($\sim 9.6 \mu\text{m}$ measured spot size) exits the catheter, enabling higher-resolution AFI. We use this system to image vascular networks in small airways in the lung periphery *in vivo* with high resolution.

Figure 1 illustrates OCT–AFI with inner-cladding excitation and core excitation. The OCT subsystem is comprised of a fiber-based Mach–Zehnder interferometer driven by a 50.4 kHz wavelength-swept source (SSOCT-1310, Axsun Technologies Inc., Billerica, Massachusetts, USA) with 20 mW output power at 1310 and 100 nm bandwidth. A balanced photodetector (PDB420C, Thorlabs, Newton, New Jersey, USA) detects the OCT signals. The AFI subsystem uses a 445 nm semiconductor laser as the excitation source and a photomultiplier tube (PMT) detector module (H9433-201, Hamamatsu, Japan) for the detection of collected autofluorescence emission. Both OCT and AFI signals are collected simultaneously on a k -clocked high-speed data-acquisition card (ATS9350, AlzarTech, Pointe-Claire, Québec, Canada) installed in a computer that processes and displays the images immediately (processing of each frame is performed much faster than the display refresh rate).

The imaging catheter fiber optic assembly consists of a length of DCF (9/105/125-20PI, FUD-3489, Nufern, East Granby, Connecticut, USA) spliced to beam-shaping fiber optics comprised of splicing step-index multimode, graded-index, and angle-polished no-core fibers, as illustrated in Fig. 1(d). This fiber assembly is fixed inside a torque cable that transfers rotational and pullback motions from the proximal end to the

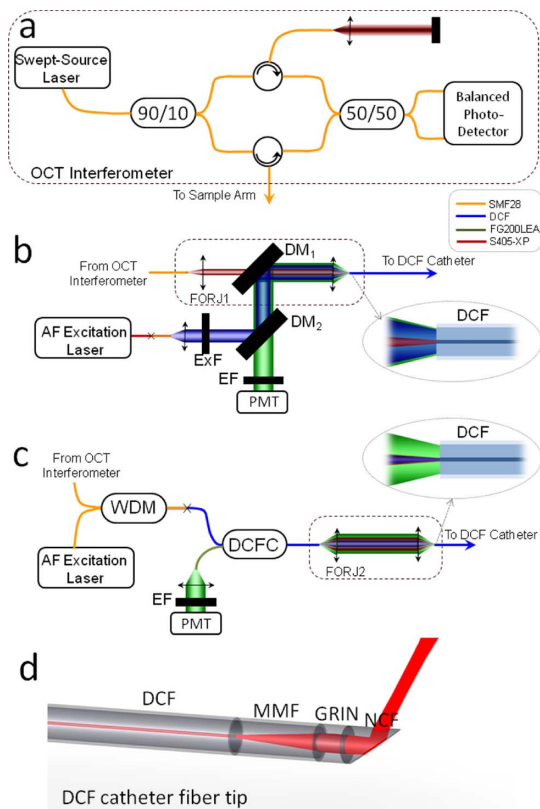


Fig. 1. OCT-AFI system schematics. (a) OCT, (b) inner-cladding AFI excitation, and (c) core AFI excitation subsystems. (d) Optical elements at the tip of the DCF catheter: DM, dichroic mirror; ExF, excitation filter; EF, emission filter; PMT, photomultiplier; WDM, wavelength division multiplexer; DCFC, double-clad fiber coupler; FORJ, fiber optic rotary joint; DCF, double-clad fiber; MMF (step-index), multimode fiber; GRIN, graded index fiber; NCF, no-core fiber.

distal end. The rotating assembly is placed inside a close-ended 900 μm diameter stationary plastic tube.

For inner-cladding AFI excitation [Fig. 1(b)], the OCT and AFI light pathways are combined using a dichroic mirror embedded in FORJ1 (DM_1). In this implementation, the OCT light is carried by the fundamental mode of the catheter's DCF core, and the AFI light (both excitation and emission) is carried by the inner-cladding modes.

For core AFI excitation [Fig. 1(c)], the OCT and AFI excitation beams are coupled through the catheter's DCF core, and the autofluorescence emission is collected through the inner cladding. The key components in this implementation are a wavelength division multiplexer (WDM, WD202A2, Thorlabs), a double-clad fiber coupler (DCFC, DC1300LEB, Thorlabs), and a custom fiber optic rotary joint (FORJ2) designed to our specifications and supplied by Princetel Inc. (Pennington, New Jersey, USA). The WDM combines the fiber-coupled semiconductor AFI excitation laser source (LP450-SF15, Thorlabs) and the OCT light in the sample arm. Using asymmetric fibers with different étendues, the DCFC has efficient coupling ($\sim 70\%$) for the light traveling through the DCF inner cladding while maintaining good isolation ($\sim 15\%$ coupling) from the DCF core [14]. This property enables separation of autofluorescence emission collected

through the catheter's DCF inner cladding from backscattered OCT light collected through the catheter's DCF core. FORJ2 couples the light to and from the rotating DCF catheter, enabling proximally driven rotational scans of the catheter's fiber assembly. Using graded-index lenses and index-matching fluid, FORJ2 couples the AFI excitation light from the stator DCF core to the rotor DCF core (similar to OCT light) and couples the AF emission collected through the DCF catheter inner cladding from the rotor DCF inner cladding to the stator DCF inner cladding to be directed to the PMT detector by the DCFC. Chromatic aberration and vibration effects are mitigated in FORJ2 using the index-matching fluid and the closely spaced graded-index lenses in the stator and the rotor sides.

Table 1 lists the measured insertion losses of WDM, DCFC, and FORJ2 with excitations and measurements at the appropriate input and output ports. For OCT and AFI excitation light, the insertion losses were measured in the forward direction through the DCF core using SMF28 patch cords. For AFI emission light, the insertion losses were measured in the backward direction using a 550 nm laser source when the DCF inner-cladding modes were excited. FORJ2 insertion loss measurements for OCT and AFI excitation optical pathways were performed through a DCF patch cord and a SMF28 patch cord to include and exclude optical power leaked into the inner cladding. Measurements indicated relatively efficient coupling from the stator DCF core to the rotor DCF core with 11% and 20% of the optical power leaking into the rotor DCF inner cladding in the OCT and AFI excitation optical pathways, respectively. The DCF core and inner-cladding excitations were also verified using a beam profiler (BeamMap2-DD, DataRay Inc., Redding, California, USA). The OCT and AFI excitation optical powers at the distal end of the catheter were 14 and 8 mW, respectively.

The AFI point spread functions (PSFs) for inner-cladding excitation and core excitation were measured to assess AFI resolution. OCT-AFI scans were performed on a phantom comprised of blue fluorescent microspheres (2 μL , 5 μm diameter, 1% solids, catalog number 2106B, Phosphorex Inc., Massachusetts, USA) suspended in water (10 mL). The phantom was imaged over 10 mm pullback with 0.6 mm/s pullback speed and 4032 A-scans/frame. Scan parameters (rotational speed and pullback speed/length) were chosen such that there were enough sampling points in the rotational and pullback directions to reconstruct the autofluorescence impulse response. A coordinate system was defined with respect to the catheter tip with r , θ , and z denoting depth, azimuthal, and pullback directions, respectively. Microspheres' distances from the catheter axis were estimated using OCT data, and the AFI PSF was obtained by measuring the FWHM of the sphere's AFI signals. Figure 2 shows exemplary autofluorescence signals and OCT of beads and FWHM measurements (panel e), including green/orange and blue/red points corresponding to inner cladding and core AFI excitations, respectively, in the azimuthal/pullback directions. Results indicate

Table 1. Insertion Losses of WDM, DCFC, and FORJ2

	445 nm	550 nm	1310 nm
WDM	0.88 dB	–	0.45 dB
DCFC	0.58 dB	1.56	0.7 dB
FORJ2	1.3 ± 0.1 dB ^a	0.26 ± 0.07 dB ^a	0.8 ± 0.1 dB ^a

^aVariation due to the rotation of the FORJ.

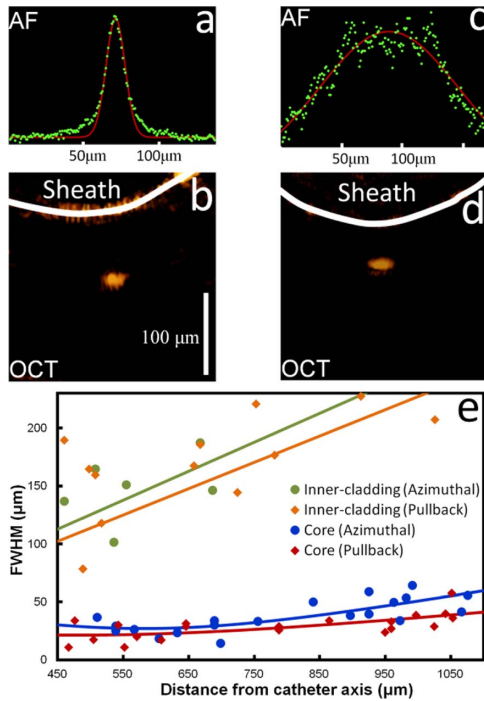


Fig. 2. AFI point spread functions. Measurement of AFI point spread functions by subresolution fluorescent beads for DCF inner-cladding and core AFI excitations. Detected autofluorescence and OCT signals of beads from DCF core (a, b) and inner-cladding (c, d) AFI excitations are shown. Results are summarized in graph (e), including green/orange and blue/red points corresponding to inner-cladding and core AFI excitations in the azimuthal/pullback directions.

significantly smaller PSF for the core AFI excitation. The PSFs increases slightly more rapidly with respect to the distance from the catheter axis in the azimuthal direction owing to the curved catheter-phantom interface in this direction. Solid lines in Fig. 2(e) indicate fits to hyperbolic functions.

In vivo OCT–AFI of human subjects was approved by the Research Ethics Board of the University of British Columbia and the British Columbia Cancer Agency. Informed consent was obtained from all participants. Optical imaging was performed during flexible bronchoscopy under local anesthesia applied to the upper airways and conscious sedation. The OCT–AFI scans added 5 to 10 min to the standard procedure time, and participants tolerated the procedure well with no adverse effects.

Figure 3 shows OCT–AFI data obtained from a segmental bronchus in the left upper lobe of an 80-year-old female using the OCT–AFI system illustrated in Fig. 1 with core AFI excitation. These data correspond to a 50 mm long pullback performed with 50 Hz rotational and 5 mm/s pullback speeds. Large vessels can be identified in the OCT structural images from the textural speckle pattern from the blood within the lumen of the vessel compared with the surrounding stationary tissue. Illustrative OCT sections corresponding to the dashed lines (panels c, d, and e) show these vessels. Identification of vessel borders can be challenging in a single OCT frame; however, adjacent frames help to discriminate vessel from neighboring tissue, as can be seen in the movie associated with this scan (Visualization 1). Vessel segmentation, as shown in the insets of Fig. 3, was carried out using several adjacent frames that include the frames shown in panels c, d, and e. These vessels correspond with features (specified by white arrows) seen in the high-resolution AFI. By extension from these large vessels, it is possible to identify networks of smaller vessels to the left

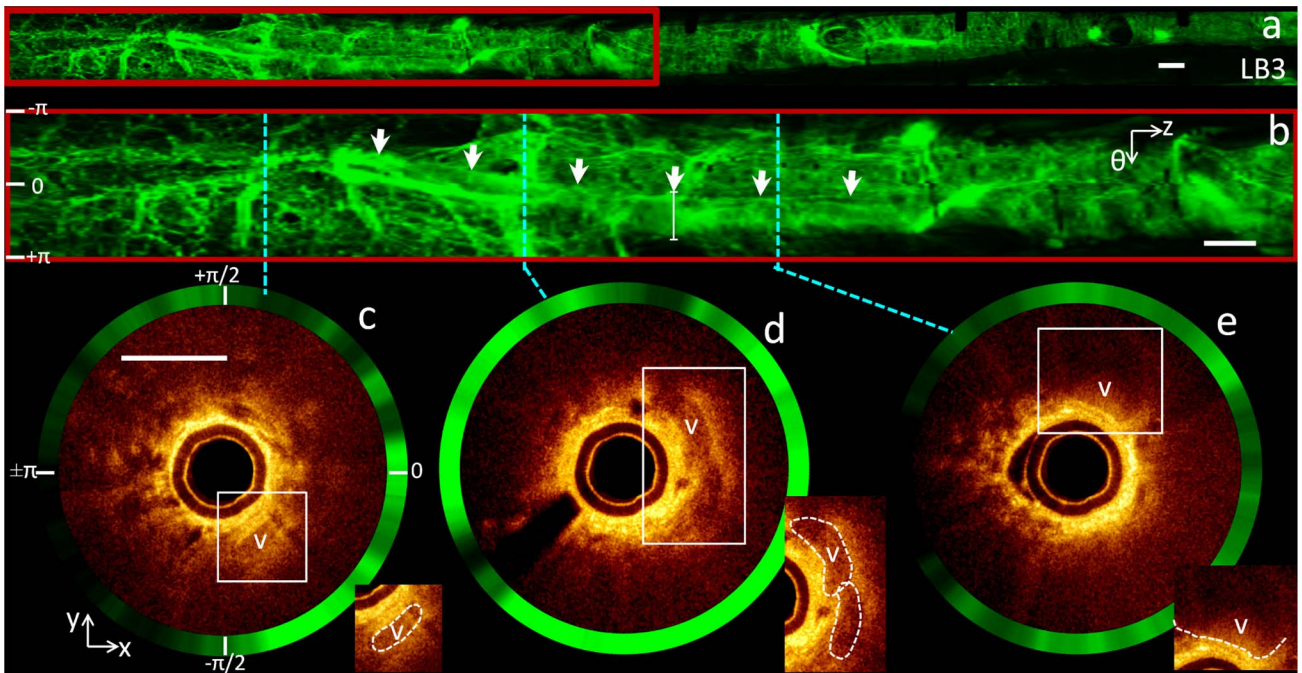


Fig. 3. *In vivo* OCT–AFI using core AFI excitation. (a) *In vivo* AFI obtained from a 50 mm pullback of an airway. (b) Magnified AFI region enclosed by the red box, and (c, d, e) OCT cross sections corresponding to the dashed lines highlight large vessels. Insets show vessel segmentation. Visualization 1 is the movie of this OCT–AFI scan. White arrows indicate a large vessel. Scale bars are 1 mm.

side of Fig. 3(b), which are not clearly identifiable in OCT imaging. We suspect other methods to identify vascular networks in the lungs, such as Doppler OCT [17], would have difficulty mapping these small vascular networks due to lower sensitivity to small, slower flowing blood vessels. Additionally, high-resolution AFI imaging can map vasculature much faster than Doppler OCT due to the high degree of A-scan oversampling required for Doppler OCT necessitating slower catheter rotational speeds. This makes AFI vascular mapping less prone to cardiac, respiratory, and clinician motion artifacts.

Figure 4 shows OCT–AFI data from two segmental bronchi in the right upper lobe (RB3a and RB3b) obtained from a 23-year-old female using core AFI excitation. Detailed vascular networks can be seen in the autofluorescence images (panels *b*, *d*, and *e*). Illustrative OCT sections in panels *a* and *c* corresponding to the white dashed lines in panel *b* show vessels that spatially correlate with the vascular pattern in the autofluorescence image in panel *b*. Illustrated in panel *e*, the magnified image of the region enclosed by the blue dashed line in panel *d* demonstrates that AFI with core excitation can visualize small vessels down to about 12 μm . The ability to visualize detailed vascular networks could provide opportunities to study angiogenesis and pulmonary vascular remodeling in different lung diseases such as lung cancer, asthma, and COPD.

Interestingly, some of the vessels imaged by AFI appear to have negative contrast (low autofluorescence intensity on a bright background) such as vessels in Fig. 4; others show positive contrast (high autofluorescence intensity on a darker background) such as vessels in Fig. 3. We hypothesize that the type of contrast depends on the type and size of vessel. Presumably, vessels that tolerate more blood pressure may require stronger walls with more fiber structures leading to stronger autofluorescence intensity. Also, large- and medium-sized vessels have tunica intima and tunica media containing highly fluorescent tissue components such as connective tissue, smooth muscle,

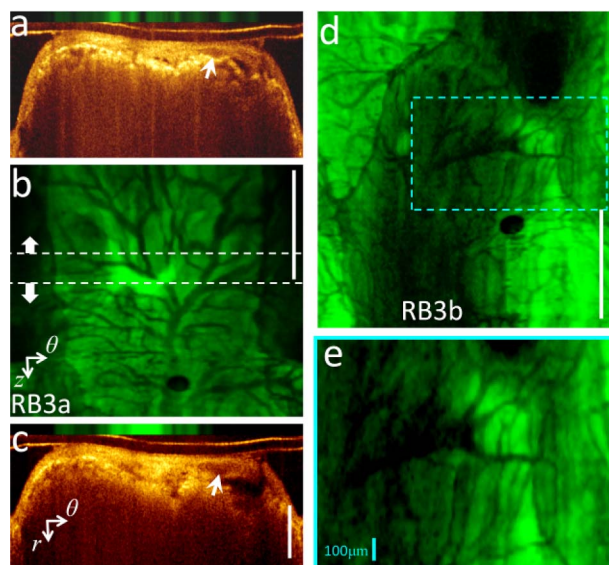


Fig. 4. Pulmonary vascular networks in high-resolution AFI. *In vivo* AFI of two normal segmental bronchi. (b) RB3a and (d) RB3b, using the system with core AFI excitation that visualizes fine pulmonary vasculature. Illustrative OCT sections (a, c) show vessels. (e) Small vessels are visualized in the magnified image. White scale bars are 1 mm.

and collagen fiber layers [18]. These vessels appear with positive contrast in AFI due to the structural protein content of their thicker walls. Smaller diameter vessels and capillaries, by comparison, only have a tunica intima comprised primarily of a thin endothelium that lacks any strong fluorescent components. These smaller vessels with no endogenous fluorophores of their own show negative contrast due to the absorption of the excitation light by blood in the lumen of the vessel and a brighter fluorescent background owing to stromal fluorescent.

This work presents *in vivo* endoscopic high-resolution AFI and co-registered OCT of peripheral airways. Using fused fiber components and a custom FORJ, the AFI excitation is coupled to the core of the DCF catheter, enabling tightly focused excitation light exiting the distal end of the catheter. Imaging subresolution fluorescent beads and airways validates the high-resolution autofluorescence imaging capability of this system. Endoscopic imaging of peripheral airways demonstrates the ability of this imaging system to visualize small pulmonary vasculature *in vivo*.

Funding. Natural Sciences and Engineering Research Council of Canada (NSERC) (PDF-453987-2014); Michael Smith Foundation for Health Research (MSFHR) (5560); Canadian Institutes of Health Research (CIHR) (345321).

REFERENCES

1. N. M. Siafakas, K. M. Antoniou, and E. G. Tzortzaki, *Int. J. Chronic Obstruct. Pulm. Dis.* **2**, 453 (2007).
2. P. Carmeliet and R. K. Jain, *Nature* **407**, 249 (2000).
3. J. L. Wright, L. Lawson, P. D. Pare, R. O. Hooper, D. I. Peretz, J. M. Nelems, M. Schulzer, and J. C. Hogg, *Am. Rev. Respir. Dis.* **128**, 702 (1983).
4. M. Wilkinson, C. A. Langhorne, D. Heath, G. R. Barer, and P. Howard, *Q. J. Med.* **66**, 65 (1988).
5. S. Y. Langenbach, L. Zheng, T. McWilliams, B. Levvey, B. Orsida, M. Bailey, T. J. Williams, and G. I. Snell, *J. Heart Lung Transplant.* **24**, 1550 (2005).
6. D. Huang, E. A. Swanson, C. P. Lin, J. S. Schuman, W. G. Stinson, W. Chang, M. R. Hee, T. Flotte, K. Gregory, C. A. Puliafito, and J. G. Fujimoto, *Science* **254**, 1178 (1991).
7. J. G. Fujimoto, M. E. Brezinski, G. J. Tearney, S. A. Boppart, B. Bouma, M. R. Hee, J. F. Southern, and E. A. Swanson, *Nat. Med.* **1**, 970 (1995).
8. G. J. Tearney, M. E. Brezinski, B. E. Bouma, S. A. Boppart, C. Pitris, J. F. Southern, and J. G. Fujimoto, *Science* **276**, 2037 (1997).
9. J. Hung, S. Lam, J. C. LeRiche, and B. Palcic, *Lasers Surg. Med.* **11**, 99 (1991).
10. S. Lam, T. Kennedy, M. Unger, Y. E. Miller, D. Gelmont, V. Rusch, B. Gipe, D. Howard, J. C. LeRiche, A. Coldman, and A. F. Gazdar, *Chest* **113**, 696 (1998).
11. T. C. Kennedy, S. Lam, and F. R. Hirsch, *Oncologist* **6**, 257 (2001).
12. H. Pahlevaninezhad, A. M. Lee, A. Ritchie, T. Shaipanich, W. Zhang, D. N. Ionescu, G. Hohert, C. MacAulay, S. Lam, and P. Lane, *Biomed. Opt. Express* **6**, 4191 (2015).
13. H. Pahlevaninezhad, A. M. D. Lee, T. Shaipanich, R. Raizada, L. Cahill, G. Hohert, V. X. D. Yang, S. Lam, C. MacAulay, and P. Lane, *Biomed. Opt. Express* **5**, 2978 (2014).
14. W. J. Madore, E. De Montigny, O. Ouellette, S. Lemire-Renaud, M. Leduc, X. Daxhelet, N. Godbout, and C. Boudoux, *Opt. Lett.* **38**, 4514 (2013).
15. D. Lorensen, X. Yang, R. W. Kirk, B. C. Quirk, R. A. McLaughlin, and D. D. Sampson, *Opt. Lett.* **36**, 3894 (2011).
16. L. Scolaro, D. Lorensen, W. J. Madore, R. W. Kirk, A. S. Kramer, G. C. Yeoh, N. Godbout, D. D. Sampson, C. Boudoux, and R. A. McLaughlin, *Biomed. Opt. Express* **6**, 1767 (2015).
17. A. M. D. Lee, K. Ohtani, C. MacAulay, A. McWilliams, T. Shaipanich, V. X. D. Yang, S. Lam, and P. Lane, *J. Biomed. Opt.* **18**, 050501 (2013).
18. M. H. Ross and W. Pawlina, *Histology: A Text and Atlas*, 6th ed. (Lippincott Williams & Wilkins, 2011).